First UV satellite observations of mesospheric water vapor

Michael H. Stevens,[1] R. L. Gattinger,[2] J. Gumbel,[3] E. J. Llewellyn,[2] D. A. Degenstein,[2] M. Khaplanov,[3] and G. Witt[3]

[1] We report the first UV satellite observations of mesospheric water vapor. The measurements are of nonthermal OH prompt emission between $300-330$ nm produced directly from the photodissociation of water vapor by H Lyman-α. This technique is most sensitive to water vapor concentrations between $70-90$ km altitude. We present OH data from two limb scanning experiments: the Middle Atmosphere High Resolution Spectrograph Investigation (MAHRSI) and the Optical Spectrograph and Infra-Red Imager System (OSIRIS). Interpretation of the lower resolution ($\sim$1 nm) OSIRIS spectra requires the rotational emission rate factors for OH(1,1) solar fluorescence between $313-318$ nm, which we present for the first time herein. Comparison of water vapor concentration profiles with the most coincident profiles from the Halogen Occultation Experiment on the Upper Atmosphere Research Satellite shows agreement to within 30% between $75-80$ km for both MAHRSI and OSIRIS. We discuss the benefits of this promising new approach to measuring upper mesospheric water vapor and the need for new laboratory measurements to improve the analysis.

1. Introduction

[2] The measured water vapor distribution in the Earth's upper atmosphere provides important details on global climate processes. Its altitude profile typically results from a balance between vertical transport and photolysis so it is an important tracer for modeling global-scale dynamics [*Smith and Brasseur*, 1991]. In addition, water vapor is the principal source of hydroxyl (OH) in the mesosphere, which is highly reactive and contributes to the catalytic destruction of ozone (O_3) [*Bates and Nicolet*, 1950; *Brasseur and Solomon*, 1986]. Moreover in the cold polar summer mesosphere water vapor forms mesospheric clouds, which have been used as diagnostics for upper atmospheric variability and for hemispheric asymmetries in climate [*Garcia*, 1989; *Chu et al.*, 2003; *Siskind et al.*, 2005; *Hervig and Siskind*, 2006; *Stevens et al.*, 2007].

[3] Despite its significance to these important dynamical, chemical and microphysical processes, satellite observations of mesospheric water vapor have only recently become available [e.g., *Harries et al.*, 1996; *Bevilacqua et al.*, 1996; *Pumphrey*, 1999; *Michelsen et al.*, 2002; *Boone et al.*, 2005; *Milz et al.*, 2005; *Lambert et al.*, 2007]. Uninterrupted global coverage is still limited, however, and observations in the vicinity of mesospheric clouds are particularly sparse [*Hervig et al.*, 2003]. Finally, previous satellite observations of mesospheric water vapor have been made at infrared and microwave wavelengths. There have been no UV satellite measurements of mesospheric water vapor to date.

[4] Mesospheric water vapor measurements can be made in the UV near 310 nm by measuring nonthermal OH $A^2\Sigma^+ - X^2\Pi$ (0,0) emission produced directly by photodissociation [*Khaplanov et al.*, 1996]. Indeed, this OH "prompt" emission has been previously observed from a comet [*Bertaux*, 1986; *Budzien and Feldman*, 1991]. We show herein OH prompt emission from the Earth's mesosphere observed by two experiments: The Middle Atmosphere High Resolution Spectrograph Investigation (MAHRSI) and the Optical Spectrograph and Infra-Red Imaging System (OSIRIS). We invert prompt radiance profiles from each experiment to retrieve volume emission rates and water vapor mixing ratios. We then compare the water vapor mixing ratio profiles from each experiment with the most coincident observations from the HALogen Occultation Experiment (HALOE) [*Russell et al.*, 1993] on NASA's Upper Atmosphere Research Satellite (UARS).

[5] We divide this work into five sections. In section 2 we define the spectral components needed to model the observations between $280-330$ nm. This includes the calculation of the OH $A^2\Sigma^+ - X^2\Pi$ (1,1) rotational emission rate factors (*g* factors) for solar fluorescence as well as the relative intensities of the nonthermal OH(0,0) and (1,1) prompt rotational emission lines. In section 3 we describe the spectral analysis used to infer the OH prompt column emission rate from the MAHRSI and OSIRIS limb spectra.

[1]Space Science Division, Naval Research Laboratory, Washington, D.C., USA.
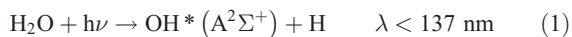[2]Department of Physics and Engineering Physics, University of Saskatchewan, Saskatoon, Saskatchewan, Canada.
[3]Department of Meteorology, Stockholm University, Stockholm, Sweden.

Report Documentation Page		*Form Approved* *OMB No. 0704-0188*

Public reporting burden for the collection of information is estimated to average 1 hour per response, including the time for reviewing instructions, searching existing data sources, gathering and maintaining the data needed, and completing and reviewing the collection of information. Send comments regarding this burden estimate or any other aspect of this collection of information, including suggestions for reducing this burden, to Washington Headquarters Services, Directorate for Information Operations and Reports, 1215 Jefferson Davis Highway, Suite 1204, Arlington VA 22202-4302. Respondents should be aware that notwithstanding any other provision of law, no person shall be subject to a penalty for failing to comply with a collection of information if it does not display a currently valid OMB control number.

1. REPORT DATE **24 JAN 2008**	2. REPORT TYPE	3. DATES COVERED **00-00-2008 to 00-00-2008**
4. TITLE AND SUBTITLE **First UV satellite observations of mesospheric water vapor**		5a. CONTRACT NUMBER
		5b. GRANT NUMBER
		5c. PROGRAM ELEMENT NUMBER
6. AUTHOR(S)		5d. PROJECT NUMBER
		5e. TASK NUMBER
		5f. WORK UNIT NUMBER
7. PERFORMING ORGANIZATION NAME(S) AND ADDRESS(ES) **Naval Research Laboratory,Space Science Division,4555 Overlook Avenue SW,Washington,DC,20375**		8. PERFORMING ORGANIZATION REPORT NUMBER
9. SPONSORING/MONITORING AGENCY NAME(S) AND ADDRESS(ES)		10. SPONSOR/MONITOR'S ACRONYM(S)
		11. SPONSOR/MONITOR'S REPORT NUMBER(S)

12. DISTRIBUTION/AVAILABILITY STATEMENT
Approved for public release; distribution unlimited

13. SUPPLEMENTARY NOTES

14. ABSTRACT

15. SUBJECT TERMS

16. SECURITY CLASSIFICATION OF:			17. LIMITATION OF ABSTRACT	18. NUMBER OF PAGES	19a. NAME OF RESPONSIBLE PERSON
a. REPORT **unclassified**	b. ABSTRACT **unclassified**	c. THIS PAGE **unclassified**	**Same as Report (SAR)**	**14**	

Standard Form 298 (Rev. 8-98)
Prescribed by ANSI Std Z39-18

In section 4 we describe the retrieval of volume emission rates and water vapor mixing ratios from the observed limb radiances. In section 5 we discuss the benefits and current limitations of this new measurement technique.

2. Emission Spectrum of OH $A^2\Sigma^+-X^2\Pi$

[6] When water vapor is photodissociated in the upper mesosphere, most of the OH produced is in the ground electronic state ($^2\Pi$). However, a small amount is produced in the electronically excited $A^2\Sigma^+$ state [*Terenin and Neujmin*, 1934], i.e.

$$H_2O + h\nu \rightarrow OH^* \left(A^2\Sigma^+\right) + H \qquad \lambda < 137 \text{ nm} \qquad (1)$$

[7] The resultant nonthermal prompt emission appears between 280–330 nm but is most apparent between 300–330 nm [*Carrington*, 1964; *Harich et al.*, 2000]. With an artificial light source, many have used this technique to obtain in situ measurements of water vapor in both the mesosphere [*Khaplanov et al.*, 1996] and the stratosphere [*Bertaux and Delannoy*, 1978; *Kley et al.*, 1979; *Schwab et al.*, 1990; *Kelly et al.*, 1993]. However, all of these measurements were made either from a balloon, an aircraft or a rocket and therefore have limited spatial and temporal coverage.

[8] OH prompt emission can also be excited in the Earth's mesosphere by solar H Lyman-α at 121.6 nm. Detection of this OH prompt emission by a satellite experiment poses two challenges. First, there is a bright underlying signal due to Rayleigh scattered sunlight that must be subtracted from the observations. Second, the solar fluorescence of the (0,0) and (1,1) bands are typically brighter than the OH prompt emission and one or both of these bands must also be removed to isolate the overlapping OH prompt lines.

[9] The MAHRSI and OSIRIS data sets require different approaches to the spectral analysis. MAHRSI observes the Earth's limb near 309 nm with a spectral resolution of 0.02 nm [*Conway et al.*, 1999], which is high enough to distinguish three discrete OH(0,0) prompt rotational lines from those due to (0,0) solar resonance fluorescence between 308.52–309.02 nm. The MAHRSI passband used herein is narrow, however, at ~0.5 nm so that the observed emission is scaled up to estimate the total OH prompt emission over several hundred OH prompt rotational lines distributed across ~30 nm based on our understanding of the intensity distribution. OSIRIS observes the Earth's limb between 280–800 nm with a spectral resolution of ~1 nm [*Llewellyn et al.*, 2004; *Gattinger et al.*, 2006, 2008], so in contrast to MAHRSI the entire rotational envelope of the OH(0,0) and (1,1) prompt emission spectrum between 300–330 nm needs to be separated from the blended (0,0) and (1,1) solar fluorescence. For both the MAHRSI and OSIRIS analyses, we require a quantitative understanding of the thermal and nonthermal OH emission lines in the Earth's upper mesosphere between 280–330 nm.

[10] In this section, we focus on the spectroscopy of mesospheric OH between 280–330 nm. We consider four major components to the OH emission spectrum: the (0,0) and (1,1) solar fluorescence bands and the (0,0) and (1,1) prompt bands. The brightest of these by far is (0,0) solar

fluorescence near 309 nm. We express the fluorescence efficiency of each transition with the g factor, which is the number of solar photons scattered per second per OH molecule. The (0,0) rotational g factors were presented and compared to MAHRSI observations by *Stevens and Conway* [1999] and are not reproduced here. We first extend the work of *Stevens and Conway* by reporting the OH(1,1) rotational g factors near 314 nm. We then report the relative intensities of the nonthermal (0,0) and (1,1) prompt rotational emission lines used in this study based on previous laboratory work [*Carrington*, 1964; *Crosley and Lengel*, 1975].

2.1. OH(1,v'') Solar Fluorescence

[11] The OH $A^2\Sigma^+-X^2\Pi$ (1,1) band is observed by OSIRIS between 313–318 nm [*Gattinger et al.*, 2006, 2008]. For solar fluorescence it is stimulated by the solar irradiance near the (1,0) transition at 280 nm. The solar irradiance is spectrally complex in the mid-UV, so that rotational transitions at nearly the same wavelength can be excited by significantly different irradiances. To derive line positions, X(0) rotational term values were taken from *Stark et al.* [1994] and A(1) term values were taken from *Coxon* [1980]. By invoking the relevant selection rules, rotational line positions for the (1,0) band were calculated and are shown in Table 1. The line positions are listed separately for each of the 12 rotational branches, where N' represents the angular momentum of the upper state apart from spin, i.e., $N' = J' \pm \frac{1}{2}$. In Table 1 and all subsequent tables, those branches with $\Delta J = J'' - J' = 0$ are Q branches, and those with $\Delta J = +1$ and -1 are P and R branches, respectively. More details of the nomenclature for each branch are provided by *Cageao et al.* [1997].

[12] For emission, X(1) rotational levels are taken from *Dieke and Crosswhite* [1962] and line positions for the (1,1) band are given in Table 2. Although only the first few rotational levels are populated for solar fluorescence in the Earth's mesosphere, we include line positions up to $N' = 20$ for the (1,1) band because they will be populated in the nonthermal prompt emission spectrum discussed in the next section.

[13] Three important differences arise when extending the OH(0,0) g factor calculation to the (1,v'') bands: the band oscillator strength (f_{10}), the branching ratio to $v'' = 1$ (ω_{11}) and the solar irradiance exciting the rotational transitions. Consistent with the recommendations of *Schleicher and A'Hearn* [1988], we take $f_{10} = 2.78 \times 10^{-4}$ [*Luque and Crosley*, 1998] and $\omega_{11} = 0.63$ [*Crosley and Lengel*, 1975]. The biggest challenge is the construction of a new solar atlas at superior spectral resolution near 280 nm.

[14] Ideally, a solar atlas with a spectral resolution higher than the Doppler width of a OH rotational line in the Earth's mesosphere (~0.001 nm) is desired to calculate the rotational g factors, which is not available. To our knowledge, the atlas with the highest spectral resolution in this wavelength range (~0.003 nm) was compiled by *Kohl et al.* [1978] and we use this as the basis for our calculations. We note that each rotational g factor is typically derived from many different absorption transitions [*Cageao et al.*, 1997; *Stevens and Conway*, 1999], effectively averaging the irradiances and reducing the uncertainty arising from the inadequate spectral resolution of the solar atlas. Later in this

Table 1. Allowed OH(1,0) Transitions[a]

N'	P_{11}	R_{11}	$^RQ_{21}$	Q_{11}	$^OP_{21}$	$^SR_{21}$	$^OP_{12}$	$^QR_{12}$	Q_{22}	$^PQ_{12}$	P_{22}	R_{22}
0	282.2532						283.7549			283.2642		
1	282.6630			281.9961	281.9986		284.3109	283.0035	283.0061	283.4966	283.4992	
2	283.0923	281.4832	281.4875	282.1497	282.1540		284.9261	282.9766	282.9810	283.7922	283.7965	282.4930
3	283.5460	281.3807	281.3866	282.3233	282.3293	280.7257	285.5954	283.0136	283.0196	284.1450	284.1511	282.2128
4	284.0281	281.2983	281.3060	282.5221	282.5298	280.3752	286.3150	283.1089	283.1166	284.5502	284.5580	281.9970
5	284.5413	281.2414	281.2508	282.7500	282.7595	280.0477	287.0820	283.2575	283.2670	285.0040	285.0136	281.8401
6	285.0879	281.2143	281.2254	283.0102	283.0214	279.7489	287.8945	283.4560	283.4672	285.5038	285.5152	281.7372
7	285.6693	281.2204	281.2331	283.3049	283.3178	279.4831	288.7512	283.7018	283.7148	286.0480	286.0612	281.6851
8	286.2869	281.2621	281.2764	283.6359	283.6505	279.2537	289.6514	283.9936	284.0082	286.6355	286.6506	281.6813

[a]Units are nm; all wavelengths for vacuum.

section, we will explore the sensitivity of our result to reductions in this spectral resolution. We note that this atlas has previously been used in the calculation of OH(1,v'') solar fluorescence of cometary OH. Although the rotational population of cometary OH is in fluorescence equilibrium rather than thermal equilibrium, spectra compare favorably to observations that resolve the rotational envelope of the bands [*Schleicher and A'Hearn*, 1988; *Budzien and Feldman*, 1991].

[15] In order to obtain the most accurate absolute solar irradiance, we normalize the *Kohl et al.* [1978] atlas to observations by the SOLar STellar InterComparison Experiment (SOLSTICE) [*Rottman et al.*, 1993] on UARS, which has an absolute accuracy of about 3.5% near 280 nm [*Woods et al.*, 1996]. We degrade the *Kohl et al.* [1978] atlas to the spectral resolution of SOLSTICE (0.3 nm) and normalize the *Kohl et al.* [1978] total irradiance between 279–289 nm to that from SOLSTICE. Using this procedure, the *Kohl et al.* [1978] absolute irradiances are adjusted downward by 27%. The result is shown over an important spectral region of excitation in Figure 1. There are some gaps in the atlas over which we interpolate and the regions of these gaps are indicated by symbols at the bottom of the figure. The gaps constitute 16% of the spectrum within the figure. Using this atlas and the transition wavelengths

indicated in Table 1, we determine the solar irradiance at each wavelength and show the results in Table 3.

[16] Following the approach described by *Stevens and Conway* [1999], *g* factors at 200 K are calculated from the irradiances in Table 3 and shown in Table 4 for the OH(1,1) band. Boldface entries indicate the brightest ten lines predicted in the (1,1) band. Summing over all rotational transitions, the vibrational band *g* factor at 200 K is calculated to be 5.3×10^{-5} s^{-1} and in excellent agreement with the estimate by *Stevens and Conway* [1999] of 5.2×10^{-5} s^{-1}. Using their 200 K *g* factor for the (0,0) band of 3.51×10^{-4} s^{-1}, the calculated (1,1)/(0,0) band ratio for solar fluorescence is therefore 0.15 and in good agreement with airglow observations by OSIRIS [*Gattinger et al.*, 2008].

[17] The predicted brightness of the (1,1) band relative to the (0,0) band is shown in Figure 2, where we have smoothed both bands with the OSIRIS spectral resolution function (~1 nm) to represent the OH solar fluorescence spectrum observed by that instrument. The (1,0) rotational *g* factors near 283 nm can be calculated by multiplying the entries in Table 4 by the A(1,0)/A(1,1) ratio measured by *Crosley and Lengel* [1975] of 0.63 and using the transition wavelengths in Table 1.

Table 2. Allowed OH(1,1) Transitions[a]

N'	P_{11}	R_{11}	$^RQ_{21}$	Q_{11}	$^OP_{21}$	$^SR_{21}$	$^OP_{12}$	$^QR_{12}$	Q_{22}	$^PQ_{12}$	P_{22}	R_{22}
0	313.8646						315.7041			315.1210		
1	314.3424			313.5480	313.5511		316.3512	314.7970	314.8001	315.3839	315.3871	
2	314.8310	312.9127	312.9180	313.7076	313.7129		317.0566	314.7410	314.7464	315.7092	315.7146	314.1669
3	315.3359	312.7574	312.7648	313.8795	313.8869	311.9782	317.8133	314.7459	314.7533	316.0894	316.0969	313.7958
4	315.8617	312.6138	312.6233	314.0692	314.0787	311.5155	318.6185	314.8080	314.8176	316.5200	316.5297	313.4892
5	316.4119	312.4882	312.4997	314.2810	314.2927	311.0693	319.4672	314.9208	314.9326	316.9960	317.0079	313.2396
6	316.9888	312.3857	312.3993	314.5185	314.5324	310.6458	320.3574	315.0819	315.0958	317.5143	317.5284	313.0433
7	317.5944	312.3108	312.3264	314.7847	314.8007	310.2500	321.2877	315.2869	315.3029	318.0729	318.0892	312.8955
8	318.2311	312.2660	312.2837	315.0817	315.0997	309.8859	322.2559	315.5344	315.5525	318.6715	318.6904	312.7938
9	318.8980	312.2541	312.2737	315.4113	315.4322	309.5570	323.2618	315.8233	315.8441	319.3069	319.3283	312.7363
10	319.5971	312.2775	312.3002	315.7740	315.7972	309.2658	324.3050	316.1522	316.1754	319.9800	320.0038	312.7243
11	320.3294	312.3365	312.3615	316.1717	316.1973	309.0156	325.3853	316.5215	316.5471	320.6906	320.7169	312.7539
12	321.0960	312.4335	312.4608	316.6057	316.6337	308.8056	326.5027	316.9313	316.9594	321.4387	321.4676	312.8269
13	321.8978	312.5700	312.5997	317.0772	317.1077	308.6390	327.6574	317.3821	317.4127	322.2249	322.2564	312.9436
14	322.7358	312.7474	312.7795	317.5874	317.6204	308.5173	328.8496	317.8744	317.9075	323.0495	323.0838	313.1047
15	323.6112	312.9673	313.0019	318.1375	318.1733	308.4421	330.0800	318.4090	318.4448	323.9134	323.9505	313.3111
16	324.5250	313.2311	313.2682	318.7290	318.7675	308.4151	331.3492	318.9868	319.0253	324.8174	324.8574	313.5638
17	325.4787	313.5403	313.5801	319.3633	319.4045	308.4378	332.6581	319.6090	319.6504	325.7626	325.8056	313.8639
18	326.4736	313.8968	313.9393	320.0418	320.0860	308.5121	334.0077	320.2769	320.3212	326.7502	326.7963	314.2129
19	327.5113	314.3022	314.3475	320.7662	320.8134	308.6395	335.3992	320.9919	321.0392	327.7816	327.8309	314.6123
20	328.5935	314.7584	314.8067	321.5385	321.5888	308.8221	336.8340	321.7557	321.8061	328.8584	328.9110	315.0638

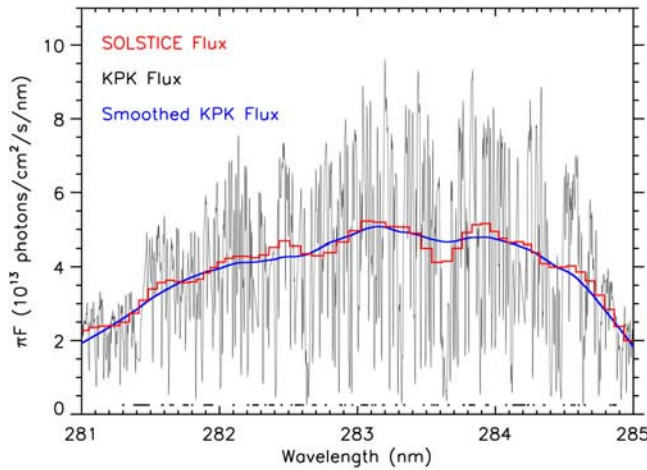[a]Units are nm; all wavelengths for vacuum.

Figure 1. Solar irradiance used for calculation of OH(1,1) g factors in this work (black). Symbols at the bottom indicate where the atlas was missing data (16% of the data in the wavelength region shown) and the atlas was interpolated over these regions. The wavelengths are for vacuum and the normalization of the high-resolution spectrum is done so that the integral of the smoothed *Kohl et al.* [1978] (KPK) spectrum (blue) is the same as that of the SOLSTICE spectrum at 0.3 nm resolution (red) between 279–289 nm. The SOLSTICE spectrum was measured on 25 February 1992.

[18] To explore the sensitivity of our results for the (1,1) vibrational band g factor on the spectral resolution of the solar atlas used, we increasingly degraded our atlas in 12 increments until the spectral resolution was equivalent to that of SOLSTICE (0.3 nm). Results are shown in Figure 3 and indicate that even though our atlas cannot resolve features down to a Doppler width of a rotational line in the Earth's atmosphere, the band g factor changes by only 6% using an atlas at lower spectral resolution. We take this as evidence that the g factor calculation is adequate for the analysis of the OSIRIS (1,1) data at 1 nm spectral resolution.

[19] The uncertainty of the OH(1,1) band g factor is driven primarily by the uncertainty of the A(1,0) Einstein coefficient, from which f_{10} is directly calculated. On the basis of the available theoretical and experimental work, we estimate this uncertainty to be ±20% [*Rouse and Engleman*, 1973; *Crosley and Lengel*, 1975; *Luque and Crosley*, 1998].

In addition, we estimate a 6% uncertainty based on our relatively low-resolution solar atlas (Figure 3), 5% for the (1,1) branching ratio [*Crosley and Lengel*, 1975], 3.5% for the solar flux near 280 nm [*Woods et al.*, 1996] and 3% for the wavelength uncertainty of the solar atlas [*Kohl et al.*, 1978]. The total root-sum-squared 1-σ uncertainty for the (1,1) band g factor is therefore ±22%. This is significantly larger than the root-sum-squared uncertainty of the (0,0) band g factor of ±7% [*Conway et al.*, 1999].

2.2. Prompt Emission

[20] As discussed earlier, when water vapor is photo-dissociated by UV light, OH is produced preferentially in the ground state. However, if the photon is energetic enough there is a small but significant quantum yield that produces OH in the $A^2\Sigma^+$ excited electronic state. The fraction of OH in the excited state depends in part on the wavelength of the photon. In the Earth's upper mesosphere where we observe most of the OH prompt emission, the photodissociation is dominated by H Lyman-α [*Nicolet*, 1984].

[21] Whereas the OH solar fluorescence spectrum in the mesosphere peaks near rotational states with angular momentum N~2 [*Cageao et al.*, 1997; *Stevens and Conway*, 1999] the OH prompt spectrum preferentially populates rotational states where N~14–22, depending on whether the $A^2\Sigma^+$ state is also vibrationally excited [*Carrington*, 1964; *Vikis*, 1978; *Okabe*, 1980]. It is this difference in the rotational population that allows us to isolate the prompt emission from the solar fluorescence.

[22] The line positions for the OH(0,0) band are shown in Table 5, which is an extension of Table 1 from *Stevens and Conway* [1999]. Table 5 uses the X(0) and A(0) term values of *Stark et al.* [1994]. The relative intensities of the rotational lines within the (0,0) and (1,1) bands are taken from *Carrington* [1964] and are shown in Tables 6 and 7, respectively, where the three lines detected by MAHRSI are highlighted in boldface. The band integrated (0,0)/(1,1) prompt ratio is discussed below.

[23] The relative brightness of the (1,1) and (0,0) prompt emission bands may be written

$$\frac{I(1,1)}{I(0,0)} = \left[\frac{N(1)}{N(0)}\right] \cdot \left[\frac{A(1,1)}{A(0,0)}\right] \quad (2)$$

where N represents the population of the $v' = 1$ or $v' = 0$ state and A(1,1) or A(0,0) is the band Einstein coefficient. The ratio of excited state populations N(1)/N(0) is 0.38 from the work of *Lee et al.* [1978]. This ratio is reflected in the ratio of the sum of the populations in Tables 6 and 7. Using

Table 3. Solar Irradiance Exciting OH(v' = 1)[a]

N'	P_{11}	R_{11}	$^RQ_{21}$	Q_{11}	$^QP_{21}$	$^SR_{21}$	$^OP_{12}$	$^QR_{12}$	Q_{22}	$^PQ_{12}$	P_{22}	R_{22}
0	3.3						6.9	2.2		5.6		
1	4.5			4.8	4.1		2.1	5.9	1.8	2.1	2.6	
2	8.0	3.6	4.1	5.4	3.3		2.1	3.1	7.5	4.0	5.0	6.3
3	7.3	2.5	1.7	4.0	4.1	1.0	2.1	4.2	6.2	3.5	4.7	4.0
4	3.1	2.2	1.8	5.2	6.2	0.6	3.8	3.1	5.1	4.7	5.9	4.7
5	6.0	2.6	2.2	4.0	5.8	1.1	6.1	3.6	5.4	1.7	1.4	2.8
6	1.2	1.9	2.8	2.9	5.1	0.4	7.7	4.7	4.8	1.3	1.9	4.3
7	2.6	2.6	2.6	2.8	0.9	0.5	8.1	4.0	5.6	6.9	5.4	3.9
8	7.9	2.4	1.6	0.8	0.9	0.9	1.9	8.6	6.4	6.6	8.9	2.3

[a]Units are 10^{13} photons/cm^2/s/nm.

Table 4. OH(1,1) g Factors at 200 K[a]

N'	P_{11}	R_{11}	$^{R}Q_{21}$	Q_{11}	$^{O}P_{21}$	$^{S}R_{21}$	$^{O}P_{12}$	$^{Q}R_{12}$	Q_{22}	$^{P}Q_{12}$	P_{22}	R_{22}
0	**3.1**						0.4			**1.8**		
1	**3.7**			**2.6**	1.5		0.5	0.8	1.3	**1.7**	1.0	
2	**4.0**	0.6	0.9	**4.1**	1.3		0.4	0.9	**2.4**	1.5	**1.9**	0.6
3	1.7	0.5	0.4	**2.1**	0.4	0.1	0.1	0.4	1.5	0.5	1.0	0.5
4	0.8	0.3	0.2	1.0	0.2	0.0	0.0	0.1	0.8	0.2	0.6	0.3
5	0.2	0.1	0.0	0.4	0.0	0.0	0.0	0.0	0.3	0.0	0.2	0.1
6	0.0	0.0	0.0	0.1	0.0	0.0	0.0	0.0	0.1	0.0	0.1	0.0
7	0.0	0.0	0.0	0.0	0.0	0.0	0.0	0.0	0.0	0.0	0.0	0.0
8	0.0	0.0	0.0	0.0	0.0	0.0	0.0	0.0	0.0	0.0	0.0	0.0

[a]Units are 10^{-6} s^{-1}; $g_{11} = 5.3 \times 10^{-5}$ s^{-1}. The ten brightest rotational lines are in boldface.

the Einstein A coefficients from *Chidsey and Crosley* [1980] we find that $A(1,1)/A(0,0) = 0.5$. This is somewhat smaller than that reported by *Crosley and Lengel* [1975] (0.6), which is limited to laboratory observations where $N' < 6$. We therefore calculate $I(1,1)/I(0,0)$ to be 0.2 in Tables 6 and 7.

[24] The modeled OH prompt spectrum between 305–330 nm is shown in Figure 4, where the relative intensities of the (0,0) and (1,1) rotation lines are shown in black and red, respectively. The entire spectrum has been smoothed using the OSIRIS spectral resolution function to simulate the observation by that instrument, analogous to Figure 2 for the solar fluorescence spectrum. The composite spectrum is overplotted as the solid black histogram. We have also indicated (in green) on Figure 4 the narrow spectral region near 309 nm where MAHRSI observes both OH(0,0) solar resonance fluorescence and three OH(0,0) relatively bright prompt emission lines. Since MAHRSI observes only a portion of the OH(0,0) prompt spectrum, we scale the observed intensities upwards to represent the prompt emission for the (0,0) and (1,1) bands. From the results shown in Table 6 and using the MAHRSI spectral resolution function over the passband shown in Figure 4, we calculate this scale factor to be 26.5.

3. The Observations

3.1. MAHRSI

[25] MAHRSI flew twice on a satellite deployed and retrieved by the crew of the space shuttle, once in 1994 and again in 1997 [*Conway et al.*, 1999]. The data used for this study are from the second mission and have been presented by *Conway et al.* [2000], who analyzed the OH(0,0) solar resonance fluorescence to retrieve OH densities in the mesosphere and upper stratosphere. We use the observations reported by *Conway et al.* to identify the relatively weak OH prompt emission because they are distinguished by smaller ($<50°$) solar zenith angles (SZAs), which allows for deeper penetration of H Lyman-α and therefore increases the mesospheric OH signal. The data are an average of 34 limb scans collected during six different orbits between 10–15 August 1997. The selected scans were taken from latitudes between 43–57°N, where the local solar time ranged between 0930–1430 and the SZA varied between 33–49°.

[26] Figure 5a shows these MAHRSI limb data in black, which is an average between 72–79 km altitude near where the OH prompt emission peaks in the mesosphere. Our spectral analysis includes the Rayleigh scattered back-

ground (in blue, top panel), the OH(0,0) solar resonance fluorescence spectrum and the OH(0,0) prompt spectrum. The OH(0,0) prompt spectrum was smoothed with the spectral resolution function of MAHRSI and included in the least squares radiance retrieval procedure discussed by *Conway et al.* [2000]. Excess emission not captured by the (0,0) solar fluorescence spectrum can be seen in the top two panels near 308.58 nm, 308.71 nm, and 309.00 nm.

[27] The effects of ozone on the shape of the background are only important near 65 km and below [*Conway et al.*, 1999], which is below where most of the OH prompt signal originates. In our analysis, we narrow the MAHRSI passband from ∼3 nm [*Conway et al.*, 2000] to ∼0.5 nm in Figure 5. Confining the passband to this spectral region reduces the uncertainty arising from imperfections in the background fitting. The passband selected (308.52–309.02 nm) includes three bright OH(0,0) prompt lines as shown in Figure 4. We then use a nonlinear least squares fitting algorithm that includes the Rayleigh scattered back-
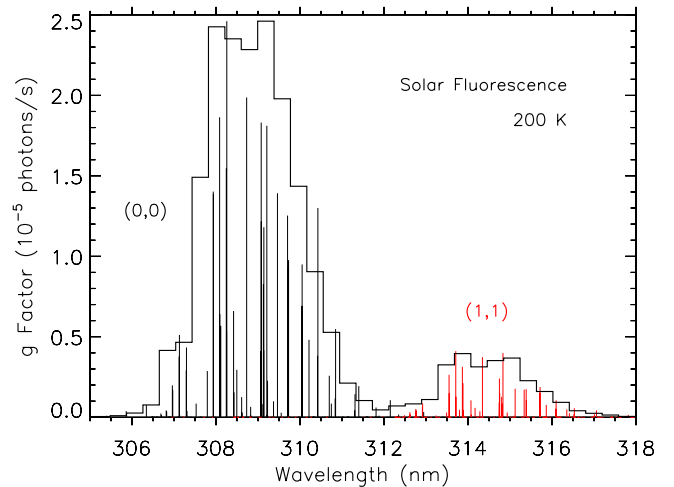

Figure 2. OH solar resonance fluorescence spectrum between 305–318 nm. The relative intensity of the (0,0) band in black is shown against the (1,1) band in red at 200 K, where the rotational emission rate factors (g factors) are indicated on the y axis. Below ∼70 km, the (0,0)/(1,1) ratio changes due to vibrational energy transfer within the upper electronic state [*Gattinger et al.*, 2008]. The entire spectrum is smoothed using the OSIRIS spectral resolution function with a full-width at half-maximum of ∼1 nm (scaled arbitrarily).
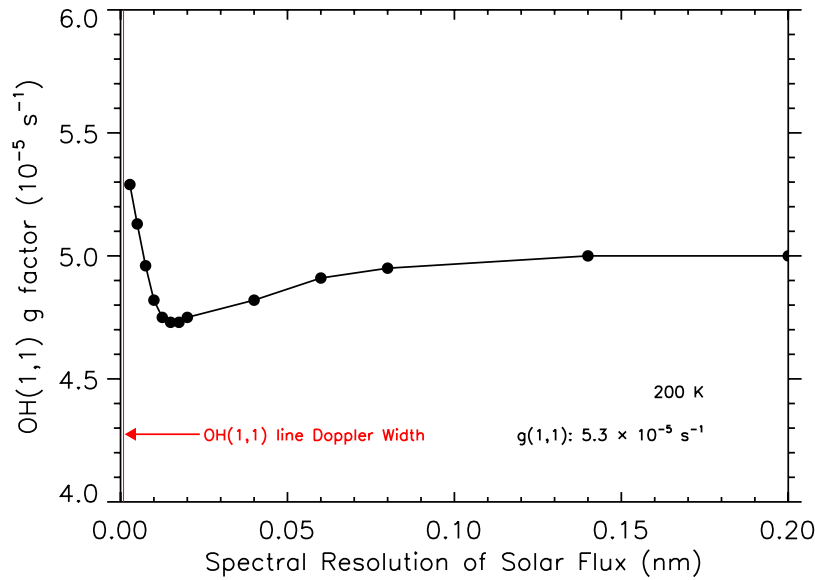
Figure 3. OH(1,1) band g factor using a solar atlas based on the observations by *Kohl et al.* [1978]. The solar atlas used in the g factor calculation does not resolve the Doppler width of a OH(1,1) rotational line in the Earth's atmosphere, but the band g factor calculated at progressively lower spectral resolutions does not change significantly.

ground, the OH(0,0) fluorescence spectrum, the OH(0,0) prompt spectrum and a constant term.

[28] In Figure 5a, the OH(0,0) solar fluorescence spectrum with the Rayleigh background fit to the data is shown in green. The composite model is in red, which includes all components of the fit, including the relatively weak OH(0,0) prompt emission. In Figure 5b the Rayleigh background has been subtracted from the data, leaving only the OH(0,0) solar resonance fluorescence and OH(0,0) prompt spectrum. The rotational branches and levels of the fluorescence lines are indicated [*Stevens and Conway*, 1999].

[29] Figure 5c shows the OH(0,0) prompt spectrum after subtracting the (0,0) fluorescence spectrum from the data in Figure 5b. Three different lines originating from high rotational levels ($N' \geq 20$) of the R_{22} and R_{11} branches are

Table 5. Allowed OH(0,0) Transitions[a]

N'	P_{11}	R_{11}	$^RQ_{21}$	Q_{11}	$^QP_{21}$	$^SR_{21}$	$^OP_{12}$	$^QR_{12}$	Q_{22}	$^PQ_{12}$	P_{22}	R_{22}
0	308.2560				307.9334	307.9366		310.0479			309.4622	
1	308.7288							310.6957	309.1351	309.1383	309.7236	309.7268
2	309.2090	307.2903	307.2956	308.0848	308.0902		311.3981	309.0710	309.0764	310.0442	310.0496	308.4944
3	309.7023	307.1208	307.1283	308.2442	308.2516	306.3411	312.1488	309.0672	309.0747	310.4170	310.4246	308.1127
4	310.2131	306.9596	306.9692	308.4174	308.4271	305.8612	312.9431	309.1168	309.1266	310.8360	310.8458	307.7923
5	310.7448	306.8133	306.8249	308.6095	308.6213	305.3937	313.7774	309.2142	309.2260	311.2966	311.3086	307.5264
6	311.2996	306.6868	306.7005	308.8239	308.8378	304.9452	314.6491	309.3548	309.3688	311.7956	311.8098	307.3093
7	311.8794	306.5842	306.5999	309.0633	309.0793	304.5211	315.5563	309.5358	309.5518	312.3308	312.3472	307.1371
8	312.4851	306.5083	306.5260	309.3295	309.3476	304.1254	316.4980	309.7549	309.7731	312.9005	312.9196	307.0070
9	313.1184	306.4614	306.4812	309.6239	309.6448	303.7613	317.4731	310.0108	310.0318	313.5042	313.5256	306.9172
10	313.7799	306.4450	306.4678	309.9483	309.9716	303.4312	318.4812	310.3033	310.3266	314.1411	314.1650	306.8673
11	314.4704	306.4615	306.4865	310.3038	310.3294	303.1377	319.5219	310.6318	310.6575	314.8111	314.8375	306.8561
12	315.1907	306.5118	306.5392	310.6912	310.7193	302.8815	320.5950	310.9964	311.0246	315.5141	315.5431	306.8840
13	315.9416	306.5975	306.6272	311.1117	311.1423	302.6645	321.7004	311.3973	311.4280	316.2503	316.2820	306.9511
14	316.7239	306.7196	306.7518	311.5663	311.5995	302.4884	322.8384	311.8349	311.8682	317.0201	317.0545	307.0581
15	317.5385	306.8795	306.9141	312.0560	312.0918	302.3544	324.0092	312.3099	312.3458	317.8240	317.8612	307.2055
16	318.3862	307.0785	307.1157	312.5819	312.6205	302.2638	325.2133	312.8229	312.8615	318.6626	318.7027	307.3942
17	319.2682	307.3178	307.3576	313.1452	313.1866	302.2182	326.4511	313.3748	313.4162	319.5366	319.5797	307.6252
18	320.1854	307.5989	307.6414	313.7471	313.7913	302.2189	327.7234	313.9666	314.0109	320.4471	320.4932	307.8995
19	321.1391	307.9232	307.9685	314.3889	314.4361	302.2674	329.0309	314.5994	314.6467	321.3949	321.4442	308.2183
20	322.1306	308.2922	308.3403	315.0720	315.1222	302.3651	330.3747	315.2745	315.3248	322.3813	322.4339	**308.5830**
21	323.1612	**308.7075**	308.7586	315.7979	315.8513	302.5137	331.7558	315.9932	316.0467	323.4077	323.4637	**308.9950**
22	324.2327	309.1708	309.2249	316.5682	316.6249	302.7149	333.1756	316.7571	316.8139	324.4754	324.5350	309.4560
23	325.3467	309.6840	309.7413	317.3848	317.4450	302.9704	334.6356	317.5679	317.6282	325.5863	325.6496	309.9677
24	326.5051	310.2490	310.3096	318.2495	318.3133	303.2821	336.1373	318.4275	318.4913	326.7420	326.8093	310.5320
25	327.7101	310.8681	310.9321	319.1646	319.2320	303.6522	337.6829	319.3379	319.4054	327.9448	328.0161	311.1509

[a]Units are nm; all wavelengths for vacuum. OH prompt lines detected by MAHRSI in boldface.

Table 6. OH(0,0) Prompt Relative Intensities[a]

N'	Rel. Pop.	P_{11}	R_{11}	$^{R}Q_{21}$	Q_{11}	$^{Q}P_{21}$	$^{S}R_{21}$	$^{O}P_{12}$	$^{Q}R_{12}$	Q_{22}	$^{P}Q_{12}$	P_{22}	R_{22}
0	0.0000	0						0			0		
1	0.0000	0			0	0		0	0	0	0	0	
2	0.0088	1031	167	250	1074	366		109	235	689	391	0	167
3	0.0095	1034	317	265	1295	273	38	86	209	924	313	533	290
4	0.0068	706	299	161	988	142	35	47	120	760	169	650	268
5	0.0066	666	342	129	1003	104	33	35	93	811	129	497	308
6	0.0066	635	372	103	1007	79	29	27	72	844	100	504	337
7	0.0066	609	393	83	1003	62	25	22	58	863	79	505	358
8	0.0077	692	480	81	1175	59	24	21	56	1031	75	502	441
9	0.0093	805	591	80	1404	58	24	19	55	1251	75	586	547
10	0.0109	918	707	81	1633	54	24	20	54	1473	74	696	657
11	0.0136	1111	886	84	2011	58	25	20	56	1829	76	808	828
12	0.0163	1283	1058	85	2355	58	27	20	57	2160	77	988	993
13	0.0201	1522	1291	90	2828	60	26	21	58	2615	82	1154	1216
14	0.0238	1744	1518	94	3281	63	27	20	59	3048	84	1380	1430
15	0.0301	2128	1891	102	4044	68	28	25	62	3779	93	1596	1793
16	0.0367	2485	2251	110	4721	69	34	23	68	4446	99	1957	2130
17	0.0539	3489	3221	143	6743	92	41	33	89	6356	133	2289	3066
18	0.0741	4593	4302	168	8956	112	56	31	107	8461	153	3250	4111
19	0.0795	4681	4468	166	9215	105	45	33	99	8727	148	4280	4274
20	0.0883	4940	4758	167	9772	100	50	36	91	9275	146	4394	**4570**
21	0.0947	5002	**4905**	161	9965	90	36	39	98	9507	137	4638	**4708**
22	0.1001	5000	4938	158	10000	99	40	41	83	9982	145	4727	4982
23	0.0159	751	751	23	1511	13	7	3	13	1589	20	4941	796
24	0.0000	0	0	0	0	0	0	0	0	0	0	783	0
25	0.0000	0	0	0	0	0	0	0	0	0	0	0	0
Total	0.72												

[a]Relative populations from *Carrington* [1964] and relative rotational lifetimes from *Chidsey and Crosley* [1980]. All intensities normalized to Q_{11}(22) at 10000. Total (0,0) intensity: 3.43×10^5. OH prompt lines detected by MAHRSI in boldface.

clearly evident and are identified in red using Tables 5 and 6. Weaker OH prompt features originating from much lower rotational levels near 308.61 nm and 308.82 nm are not evident above the noise. The integrated brightness of the prompt radiance within the passband shown is indicated in the upper right of Figure 5c. Using our scale factor (26.5) derived from results shown in section 2, we find that the total OH(0,0) + (1,1) prompt radiance between 72–79 km is 42 kiloRayleighs (kR), where 1 kR is the apparent emission rate of 10^9 photons/cm^2/s.

Table 7. OH(1,1) Prompt Relative Intensities[a]

N'	Rel. Pop.	P_{11}	R_{11}	$^{R}Q_{21}$	Q_{11}	$^{Q}P_{21}$	$^{S}R_{21}$	$^{O}P_{12}$	$^{Q}R_{12}$	Q_{22}	$^{P}Q_{12}$	P_{22}	R_{22}
0	0.0000	0						0			0		
1	0.0117	710			500	357		95	147	296	333	242	
2	0.0115	600	95	148	618	217		66	135	398	232	308	97
3	0.0111	526	157	138	650	143	19	45	106	467	164	329	146
4	0.0113	507	208	119	699	106	25	35	87	540	126	357	189
5	0.0113	490	243	98	726	80	25	27	70	591	98	372	222
6	0.0115	474	270	80	739	61	23	22	56	624	77	379	246
7	0.0117	474	293	68	765	50	19	17	45	664	63	392	271
8	0.0122	472	315	57	787	42	17	15	38	696	54	402	292
9	0.0132	491	342	51	835	37	15	12	33	750	47	427	321
10	0.0143	518	378	47	899	32	14	11	29	820	43	459	357
11	0.0167	581	436	45	1020	31	14	11	29	940	42	522	415
12	0.0213	711	550	49	1267	33	15	10	30	1178	44	645	527
13	0.0226	722	572	47	1298	30	14	11	25	1272	39	693	571
14	0.0237	725	587	43	1315	29	11	7	22	1300	34	704	589
15	0.0237	689	566	38	1259	23	11	7	19	1327	30	711	605
16	0.0217	594	496	34	1097	19	8	7	14	1285	24	688	593
17	0.0143	373	312	25	689	18	7	2	9	1150	13	613	530
18	0.0098	243	207	11	452	8	4	2	5	583	8	309	269
19	0.0035	83	71	3	155	2	1	1	2	156	2	82	72
20	0.0019	40	34	1	75	1	0	0	1	75	1	40	35
Total	0.28												

[a]Relative (1,1) rotational population based on *Carrington* [1964]. $v' = 1$ population based on *Lee et al.* [1978] and normalized to populations in Table 6 so that N($v' = 1$)/N($v' = 0$) = 0.38. Total OH(1,1) prompt intensity normalized to (0,0) intensity in Table 6 so that I(0,0)/I(1,1) = 5.1. Rotational Einstein A coefficients from which intensities calculated are from *Chidsey and Crosley* [1980], where A(1,1) is based on the calculated A(1,1)/A(0,0) ratio of *Crosley and Lengel* [1975] at lowest rotational levels.
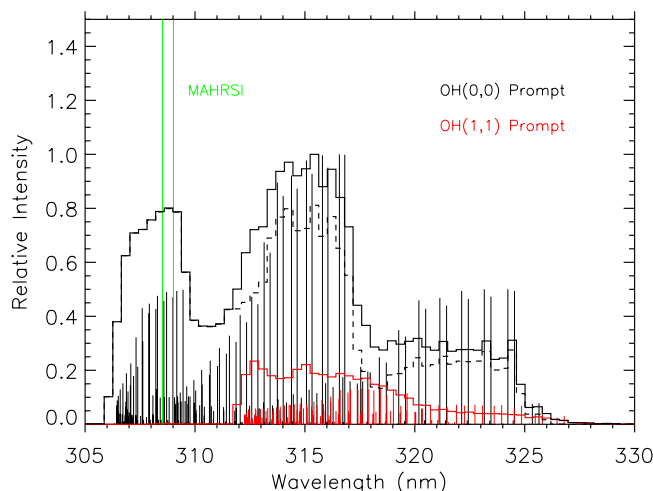
Figure 4. OH prompt fluorescence spectrum between 305–330 nm. The relative intensity of the (0,0) rotational spectrum is shown against the (1,1) spectrum. The spectrum is smoothed using the OSIRIS spectral resolution function with a full-width at half-maximum of ∼1 nm and the resultant (0,0) spectrum is shown as the black dashed histogram, the (1,1) spectrum is shown as the red histogram and the composite of the two is shown as the black solid histogram (arbitrarily scaled). The (0,0) spectrum is a factor of five brighter than the (1,1) spectrum and the region of the OH prompt spectrum observed by MAHRSI is indicated in green.

[30] We employ this procedure at each 2 km altitude step to retrieve the OH(0,0) + (1,1) radiances between 65–85 km and the results are shown as the black curve in the left hand panel of Figure 6. Uncertainties (1σ) are shown as the darker shaded envelope and do not include systematic uncertainties such as those for the g factor. We invert these radiances to retrieve the volume emission rates (VERs) as a function of altitude and these are overplotted as the red curve and referenced to the top axis, where the statistical uncertainties are propagated through the inversion and shown as the lighter shaded region beneath the red curve. For this inversion we have included a small amount of extinction by ozone at the lowest altitudes shown [*Gattinger et al.*, 2006] but have assumed that quenching and vibrational energy transfer of the excited state is negligible. We see that the emission increases sharply from 85–75 km due to the increasing water vapor concentrations at these altitudes and then decreases from 75–65 km due to the attenuation of the solar H Lyman-α flux. We will model these processes in section 4.

3.2. OSIRIS

[31] OSIRIS was launched aboard the Odin satellite [*Murtagh et al.*, 2002] on 20 February 2001 with an orbital inclination of 98°. Odin is in a sun-synchronous orbit with equator crossing times near 0600 and 1800 local time so that OSIRIS observes the Earth's limb both near sunrise and sunset [*Llewellyn et al.*, 2004]. The instrument measures atmospheric limb scattered solar radiation over the wave-

length range from 274 nm to 810 nm with 1 nm spectral resolution. The vertical field of view is 1 km at the tangent point and the vertical sampling interval is approximately 1.5 km. The on-orbit instrument absolute calibration is based on solar flux data from the Solar Ultraviolet Spectral Irradiance Monitor database [*Brueckner et al.*, 1993] and a multiple scatter atmospheric model.

[32] As with the MAHRSI analysis [*Conway et al.*, 1999], an accurate estimate of the atmospheric background spectrum is required to isolate the OH bands [*Gattinger et al.*, 2006]. The procedure adopted here is to first subtract a scaled 60 km Rayleigh scattered atmospheric background spectrum from the upper mesospheric spectra and then to subtract a scaled spectrum above the OH optical emission region, averaged over the 92 to 94 km range, to remove the thermospheric dayglow component [e.g., *Cleary et al.*, 1995] and a weak baffle scatter component present at wavelengths longer than approximately 315 nm.

[33] Since the total OH solar fluorescence is typically much brighter than the prompt emission, we limit our observations to those from the early morning (0700–0800 local time). At this part of the day the OH has not yet accumulated through photodissociation so the OH fluorescence is relatively weak [*Gattinger et al.*, 2006]. Since the OH prompt emission is produced directly by the photodissociation of upper mesospheric water vapor by H Lyman-α we do not expect it to have the strong diurnal dependence of the OH solar fluorescence.

[34] Figure 7a shows an OSIRIS limb spectrum and the estimate of the Rayleigh background spectrum scaled to the data and overplotted in red. The limb spectrum is composed of an average of 42 scans between 50–70°N on 3–4 June 2005. The excess emission near 308 nm and 315 nm is due to OH(0,0) and (1,1) solar fluorescence and prompt emission. Figure 7a serves to illustrate that in general the OH signal is less than 10% of the total limb emission observed at 80 km. The spectrally complex background is fit extremely well away from the OH emission, underscoring its reliability where we infer the signal.

[35] Figure 7b shows the OSIRIS data from Figure 7a with the Rayleigh scattered background removed. Overplotted on the data are the results of a least squares fitting algorithm, which uses the theoretical OH(0,0) and (1,1) g factors convolved with the OSIRIS spectral resolution function (blue), the OH(0,0) and (1,1) prompt spectrum at OSIRIS resolution (green) and the composite fit to the data (red). The composite fit to the data is excellent and the emission between 320–325 nm demonstrates that OH prompt emission is detected. The total OH(0,0) + (1,1) prompt radiance inferred at 80 km is 43 kR and indicated in green in Figure 7b.

[36] Figure 7 also serves to illustrate that the spectral resolution of OSIRIS (∼1 nm) is such that the OH(0,0) and (1,1) fluorescence and prompt components are blended together. Since the uncertainty of the (1,1) g factor is relatively large at 22% (section 2.1), we considered how the retrieved OH(0,0) + (1,1) prompt emission varied with a 15% reduction in the (1,1) g factor. We find that the OH prompt intensity increases by only 5–10% near the peak ∼80 km, which is approximately the statistical uncertainty shown in Figure 6. This is small in the context of our initial
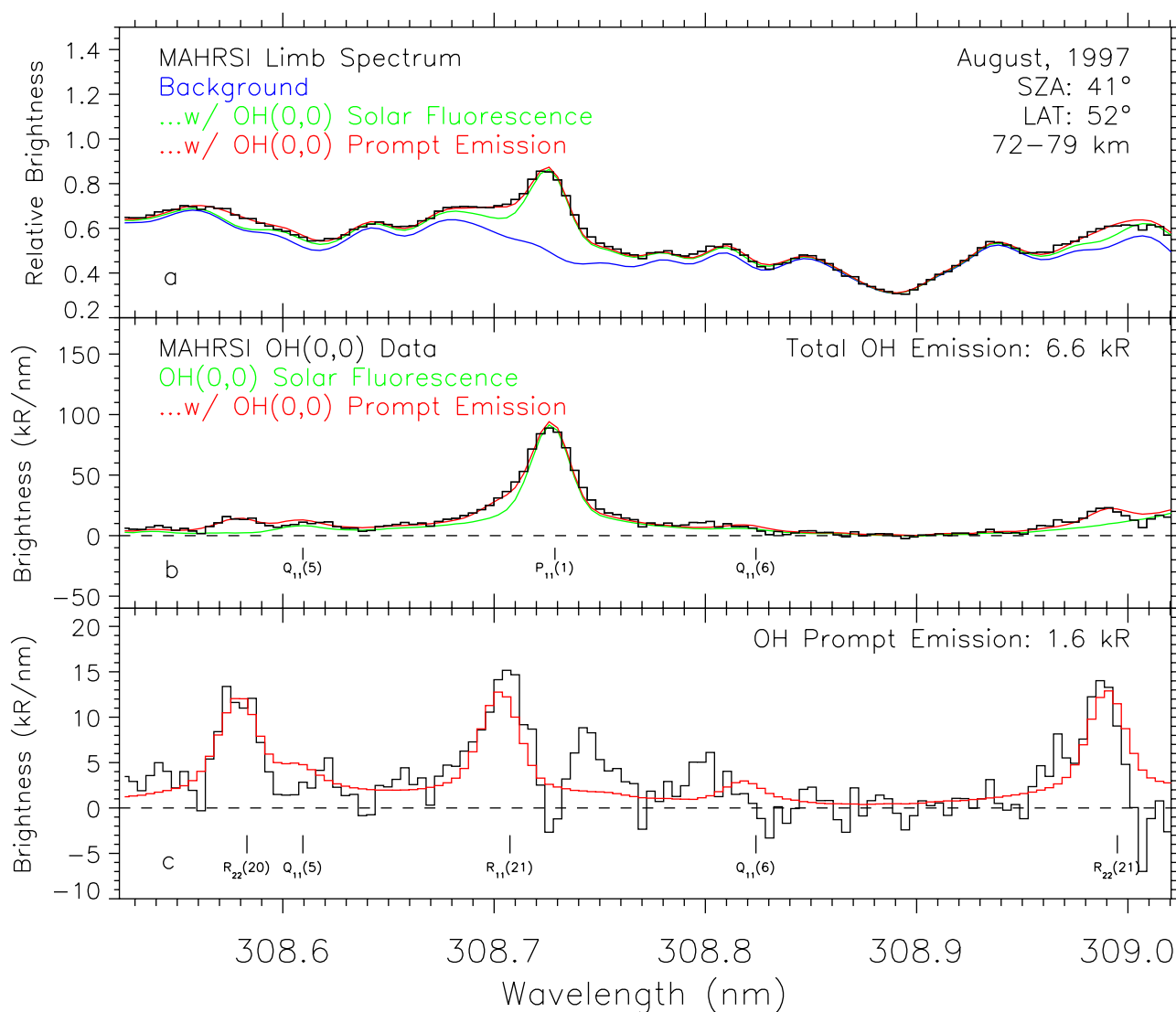
Figure 5. (a) MAHRSI limb spectrum from August 1997. The data shown are an average of 34 scans yielding a total integration time of about $2\frac{1}{2}$ min. The data are shown as a black histogram and the estimated Rayleigh scattered background is scaled to the data and shown in blue. The OH(0,0) solar resonance fluorescence is shown on top of the Rayleigh background in green and the composite fit including the OH(0,0) prompt emission spectrum is shown in red. Average properties of the observation set are shown in the upper right. (b) Same as Figure 5a but with the Rayleigh background subtracted. The most important (0,0) solar resonance fluorescence lines are modeled at 200 K and indicated with the angular momentum of the upper state in parentheses. (c) Same as Figure 5b but with the OH(0,0) solar resonance fluorescence contribution subtracted, revealing the OH prompt emission spectrum.

study, but underscores the need to constrain A(1,0) in laboratory studies to improve our retrievals.

[37] We similarly fit the fluorescence and prompt components of OH to the limb data at other altitudes and infer the OH prompt radiance profile. The results are shown in the right hand panel of Figure 6 in black with the statistical error envelope shaded (1σ). We invert these radiances to derive VERs, which are overplotted in red and referenced to the top axis. Overall, the OSIRIS VERs are similar to MAHRSI's in the left hand panel. The peak is a slightly higher altitude (near 78 km) compared to MAHRSI (75 km), which is probably due to the larger solar zenith angle for the OSIRIS observations and a different vertical distribution of

water vapor for the conditions indicated. We will explore these differences in the next section.

4. Modeling Approach

[38] We now model the VERs shown in Figure 6 in order to derive the water vapor mixing ratio profiles. We simulate the lighting conditions of each set of observations and use water vapor concentrations inferred from HALOE observations that are as close as possible in time and space to our observations.

[39] For this analysis, we focus on the altitude region between $65-90$ km where there is measurable signal from the satellite observations. We also assume that the solar H
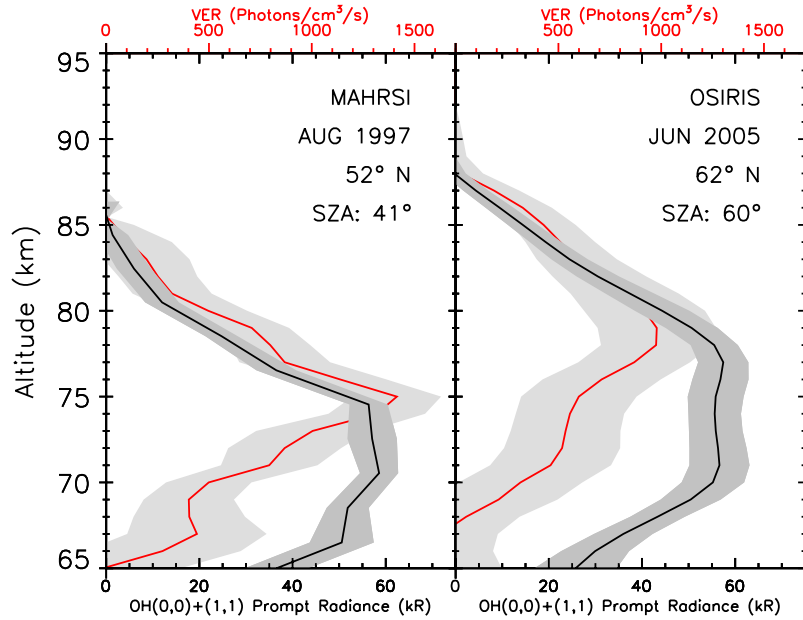
Figure 6. MAHRSI (left) and OSIRIS (right) OH prompt observations in the upper mesosphere. Black curves indicate the observed OH(0,0) + (1,1) limb radiances with 1σ statistical uncertainties indicated. Shown in red are the volume emission rates determined from an inversion of each radiance profile and referenced to the top axis. Solar zenith angles (SZA) for each set of observations are indicated.

Lyman-α flux is the only source of OH prompt emission in the Earth's upper mesosphere. The volume emission rate (P) can be expressed as

$$P(z) = \sigma_\lambda \cdot \phi \cdot \Psi_\lambda(z) \cdot [H_2O(z)] \quad (3)$$

where $\psi_\lambda(z)$ is the H Lyman-α flux at each altitude level, ϕ is the OH(0,0) + (1,1) prompt yield, σ_λ is the water vapor cross section and $[H_2O(z)]$ is the water vapor concentration [*Gumbel*, 1997]. In our modeling approach, we neglect quenching of the $A^2\Sigma^+$ state as well as vibrational energy transfer (VET) and rotational energy transfer (RET), which become important below ∼65 km [*Conway et al.*, 1999; *Gattinger et al.*, 2008]. Available laboratory results indicate, moreover, that quenching and RET are less efficient at high rotational levels ($N' = 16-20$) than at low rotational levels ($N' < 3$) [*Kaneko et al.*, 1968; *Copeland et al.*, 1985; *Papagiannakopoulos and Fotakis*, 1985; *Burris et al.*, 1991; *Gumbel*, 1997]. As indicated in section 3.1, extinction due to ozone is not important above 65 km [*Conway et al.*, 1999] and is therefore not included in our model simulations. We discuss the inputs to equation (3) in order now.

[40] Although molecular oxygen (O_2) controls the attenuation of solar H Lyman-α in the upper mesosphere, the water vapor cross section is required to model the observed OH prompt volume emission rate in equation (3). To determine the average cross section of water vapor, σ_λ, we model the shape of the solar H Lyman-α line between $121.467-121.667$ nm in 0.001 nm increments [*Chabrillat and Kockarts*, 1997]. We normalize that to unity and integrate over the cross sections as given by *Lewis et al.* [1983]. This yields an average cross section of 1.51×10^{-17} cm^2.

[41] There is currently some ambiguity for the OH prompt yield, φ. *Carrington* [1964] reported a yield of

0.05 with uncertainty of a factor of two to three. *Lee and Suto* [1986] gave a value of 0.075 near Lyman-α with and uncertainty of 30%. On the other hand, *Harich et al.* [2000] find that there is an even larger 0.13 yield to OH prompt following photodissociation by H Lyman-α. Given this ambiguity we consider two possible yields: 0.075 and 0.13. From equation (3), the yield directly affects our volume emission rate calculation so we will consider the impact of each on our comparison. We assume that OH prompt emission appears exclusively in the (0,0), (1,1), and (1,0) bands. Since we only model the (0,0) and (1,1) bands herein, we reduce the reported yield slightly to account for the rest of the emission lost to (1,0). We have determined that I(1,1)/I(0,0) is 0.2 in section 2.2. On the basis of the experimental work of *Crosley and Lengel* [1975], the A(1,0)/A(1,1) ratio is 0.63 so that the yields used in our analysis are reduced by 9% to 0.068 and 0.118.

[42] To derive the solar H Lyman-α flux with altitude, we first determine the flux appropriate to the day of the MAHRSI (12 August 1997) and OSIRIS (4 June 2005) observations. This is obtained using the compilation at the LASP Interactive Solar Datacenter (http://lasp.colorado.edu/LISIRD/). We find that during the MAHRSI OH observations, the solar H Lyman-α flux was 3.73×10^{11} photon/cm^2/s whereas for the OSIRIS observations it was 3.93×10^{11} photon/cm^2/s. We assume that the attenuation of Lyman-α is entirely due to the overhead column of O_2, which has a well-known window near 121.6 nm allowing for the penetration of H Lyman-α to the upper mesosphere [e.g., *Lewis et al.*, 1983]. We parameterize the absorption following the approach described by *Chabrillat and Kockarts* [1997, 1998]. For the O_2 column we use the HALOE background atmosphere and the O_2 mixing ratio as a function of altitude from the empirical atmospheric model NRLMSISE-00 [*Picone et al.*, 2002]. As discussed previ-
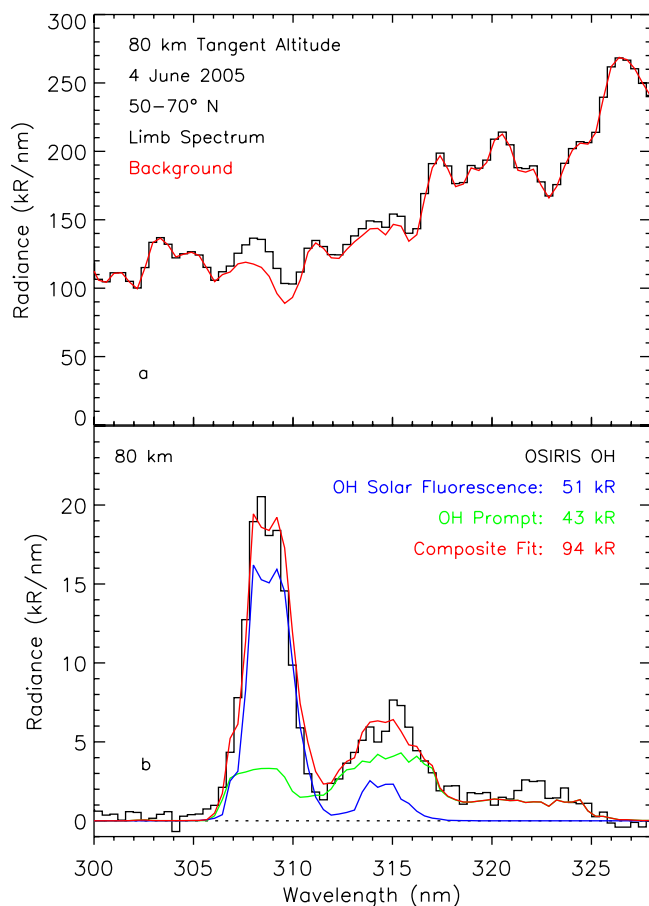
Figure 7. (a) OSIRIS limb spectrum (black) with an estimate of the Rayleigh scattered background brightness fit to the data (red). The data are a 42 scan average from a tangent altitude of 80 km between 50–70°N on 3–4 June 2005. (b) The OSIRIS OH spectrum at 80 km obtained from subtracting the Rayleigh background spectrum from the data in Figure 7a. A least squares fit of OH(0,0) + (1,1) prompt emission (green), OH(0,0) + (1,1) solar fluorescence (blue) and the composite fit (red) to the data are shown with their integrated radiances indicated.

ously, the amount of absorption is sensitive to the solar zenith angle and we use the average zenith angle for each data set in our calculations.

[43] Results are shown in Figure 8a for MAHRSI conditions and Figure 8b for OSIRIS conditions. Note the higher altitudes of extinction for the OSIRIS case, which is due to the larger solar zenith angle indicated in each figure. In general, Figure 8 shows that the OH prompt emission should decrease above 75–80 km because of lower water vapor concentrations and should decrease below these altitudes due to the reduction of available H Lyman-α radiation (see Figure 6).

[44] For comparison against our results we use the HALOE background atmosphere and water vapor profiles most coincident in space and time. For the MAHRSI analysis, we coverage 59 HALOE profiles from 22–23 July and 2–3 September 1997, which are before and after the MAHRSI observations on 10–15 August. The average latitude of these HALOE scans was 50°N (compared to the

MAHRSI latitude of 52°N) and the uncertainty of the coaveraged profile is indicated by the shaded area in Figure 8a and referenced to the top (red) axis. Above 85 km the HALOE data are highly uncertain so we show this region with a dotted line hereinafter in model calculations.

[45] For the OSIRIS analysis, 60 HALOE scans were co-averaged between 4–8 June 2005 near 65°N (compared to OSIRIS at 62°N). PMCs can bias the HALOE water vapor measurements [*McHugh et al.*, 2003], but the PMC signature in the OSIRIS data for these latitudes for this early in the PMC season was very weak. The resultant coaveraged water vapor profile is overplotted with a shaded uncertainty in Figure 8b. Note that the water vapor extends to higher altitudes in Figure 8b compared to Figure 8a, as expected at the higher latitudes during June.

[46] Using the HALOE water vapor concentrations and the H Lyman-α flux shown in Figure 8, we calculate the VERs from equation (3) for two different yields and the results are shown in Figures 9a and 9b. The VERs of MAHRSI and OSIRIS are reproduced from Figure 6 for direct comparison and the model uncertainties are propagated directly from the uncertainties in the HALOE water vapor profiles in Figures 8a and 8b. The agreement for each data set is remarkable, particularly since the HALOE observations are not precisely colocated in space and time with those from either MAHRSI or OSIRIS. Both data sets clearly favor the larger yield of 13% reported by *Harich et al.* [2000].

[47] Using the observed VERs (Figure 9) and the H Lyman-α flux (Figure 8), equation (3) can be solved for the water vapor concentration. By taking the number densities of the background atmosphere from the HALOE measurements in Figure 8, we show the retrieved water vapor mixing ratio profiles in Figure 10. The vertical resolution of the HALOE profiles is 3–5 km [*McHugh et al.*, 2005] and the vertical resolution of both the MAHRSI and OSIRIS water vapor profiles is about 4 km. The MAHRSI results in Figure 10a show excellent agreement with HALOE water vapor, despite the fact that a direct comparison with data from the same month and latitude is not possible. Between 70–80 km, we find that the agreement is within 30% of HALOE observations. Figure 10b shows the comparison between OSIRIS and HALOE and the agreement between 75–85 km is also within 30% of HALOE. Below 74 km the OSIRIS data are well in excess of the HALOE data and are not shown. Inspection of Figure 9b shows that the VERs are systematically higher than the HALOE data and this difference propagates directly to the retrieved mixing ratios. The difficulty in retrieving water vapor by OSIRIS below 74 km is reflected in the uncertainties shown by the shaded area in Figure 9 (right).

5. Discussion and Summary

[48] We have reported the first UV satellite observations of water vapor in the Earth's mesosphere. These observations of OH prompt emission near 310 nm come from two separate experiments. The measurement is challenging because the prompt emission is weak compared to both the Rayleigh scattered background and the OH(0,0) and (1,1) solar fluorescence in the spectral region between 300–330 nm. In order to help distinguish between the
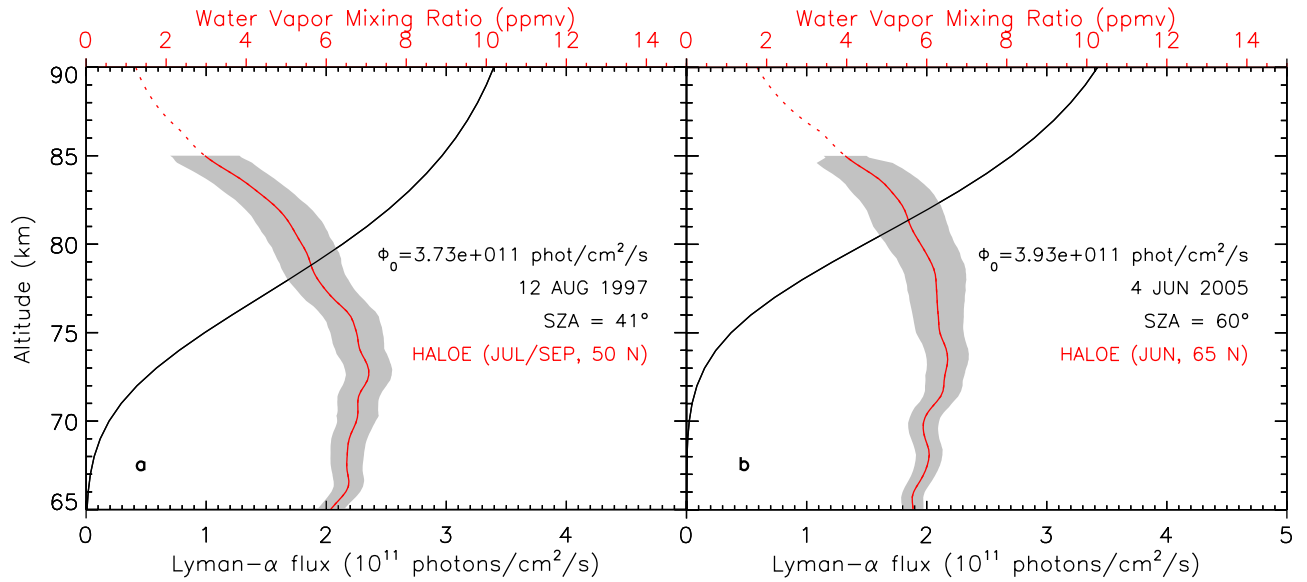
Figure 8. Solar Lyman-α fluxes (in black) used for the analysis of (a) MAHRSI and (b) OSIRIS OH prompt emission data. The fluxes at the top of the atmosphere for the indicated dates are shown. Also shown (in red, referenced to the top axis) are averaged HALOE water vapor profiles from July and September 1997 (MAHRSI) and June 2005 (OSIRIS) at latitudes indicated in red. The HALOE profiles are most coincident in space and time with the MAHRSI and OSIRIS results presented herein. The HALOE data above 85 km have large uncertainties and this portion of the profile is shown as a dotted line.

blended emissions within this region, we have calculated the OH(1,1) rotational g factors for solar fluorescence in the Earth's mesosphere and reported them here for the first time in Tables 2 (line positions) and 4 (g factors). We have also reported line positions and predicted relative intensities of OH(0,0) and (1,1) prompt rotational emission lines in Tables 2, 5, 6, and 7 on the basis of previous laboratory measurements of the rotational populations [Carrington,

1964] and transition probabilities [Crosley and Lengel, 1975].

[49] Our two data sets offer separate benefits in the analysis and approach. MAHRSI uses higher spectral resolution (0.02 nm) with a narrower passband (0.5 nm) whereas OSIRIS uses lower spectral resolution (1 nm) across a wider passband (more than 30 nm). Because the rotational distribution of the OH prompt emission is non-
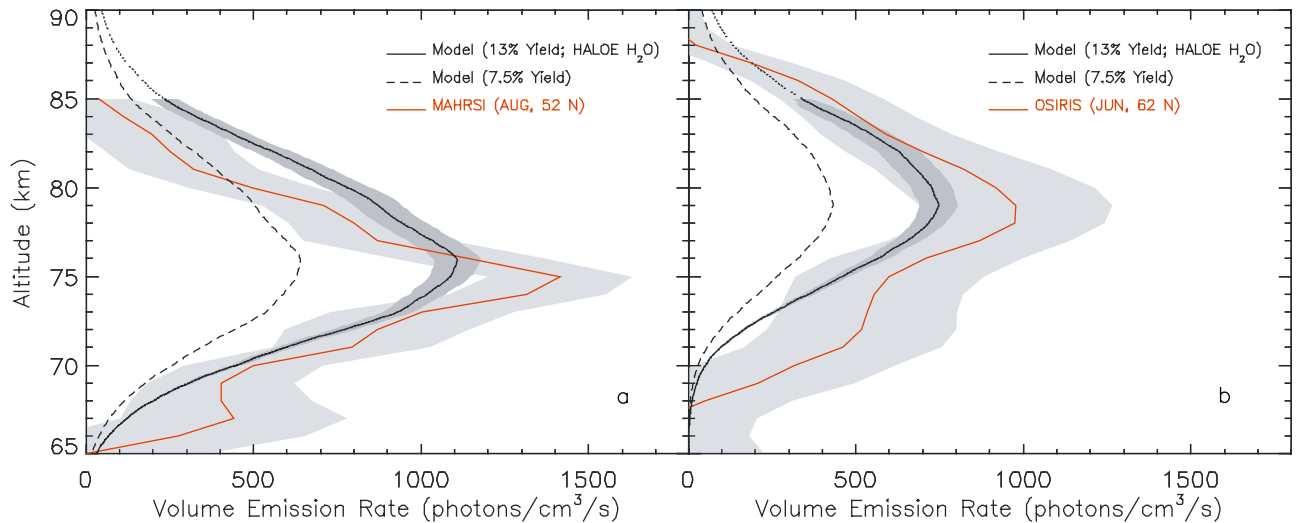

Figure 9. Calculated OH(0,0) + (1,1) prompt volume emission rates in solid black using a yield of 13% for conditions of (a) MAHRSI and (b) OSIRIS. The error envelope reflects the uncertainty in the HALOE water vapor profiles shown in Figure 8. Model results above 85 km rely on uncertain HALOE water vapor retrievals at these altitudes so these results are shown with a dotted line. The volume emission rates from Figure 6 are overplotted for comparison. Also shown for comparison in dashed black is the model result for a yield of 7.5%. Both data sets are most consistent with a 13% yield.
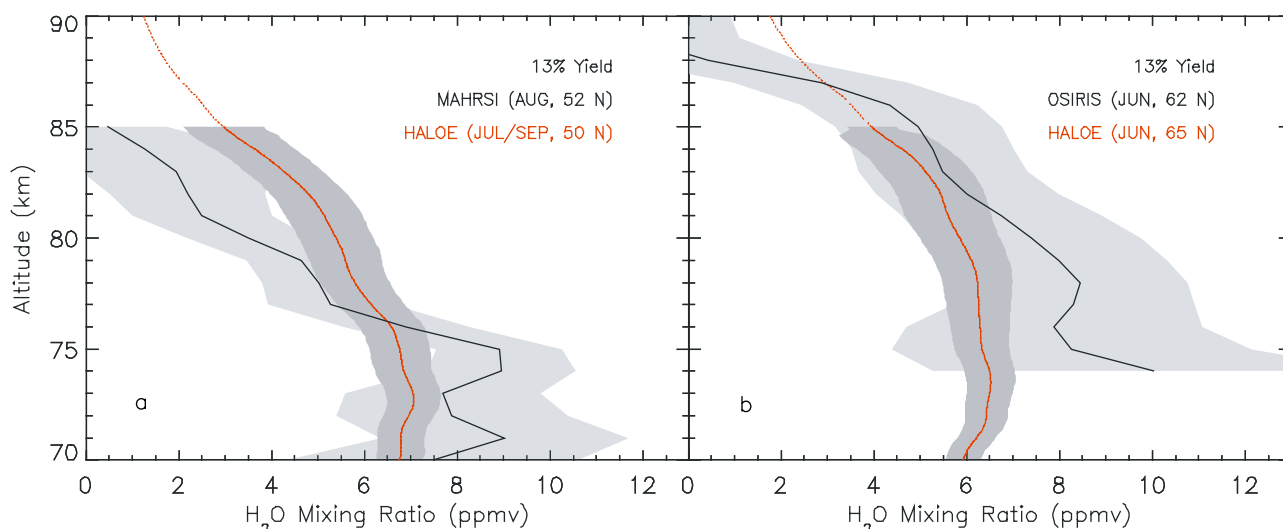
Figure 10. Water vapor retrievals from (a) MAHRSI and (b) OSIRIS in black. HALOE profiles from Figure 8 are overplotted for comparison. For both data sets, agreement is within 30% of HALOE results between 75–80 km altitude using the indicated yield.

thermal and therefore a separate population from solar fluorescence, it is distinguishable either through individual rotational transitions (MAHRSI, Figure 5c) or the shape of the rotational envelope (OSIRIS, Figure 7b).

[50] We show only a limited amount of data herein to emphasize the new approach rather than to provide a database of mesospheric water vapor observations. MAHRSI and OSIRIS observations agree to within 30% of HALOE observations between 75–80 km where the OH prompt radiance peaks. We find that a yield of 13% for OH prompt emission from the photodissociation of water vapor by H Lyman-α [Harich et al., 2000] is most consistent with both the MAHRSI and OSIRIS data. New laboratory work constraining the OH prompt yield following photodissociation by H Lyman-α is needed given the current ambiguity in the literature, where this value varies between 5–13%. In addition, precise measurements of the rotational distribution would benefit high-resolution measurements such as MAHRSI, which has a limited passband so that the analysis relies on a large scaling for the vibrational band intensity. Finally, tighter constraints on the lifetime of the $v' = 1$ state would benefit measurements at lower resolution such as OSIRIS, which must separate the blended (0,0) and (1,1) fluorescence and prompt components. Nonetheless, the excellent agreement between these two diverse data sets with validated HALOE observations [Harries et al., 1996; McHugh et al., 2005] underscores the reliability of our water vapor retrievals.

[51] It is unlikely that OH prompt emission could provide robust water vapor retrievals below 65 km because not only do quenching and ozone extinction become important below this altitude, but H Lyman-α is attenuated below 75 km and severely reduces the observed prompt emission (Figure 6). Above 75 km, the emission becomes weaker due to the strong decrease of water vapor concentrations with altitude. However, the technique shows promise for quantifying the water budget in the polar summer mesosphere, where concentrations are more elevated and for which few water vapor measurements currently exist.

[52] Since the OH prompt measurement is made from airglow observations rather than occultation, it is more synoptic and could ultimately provide daily global maps of upper mesospheric water vapor. Although MAHRSI was a shuttle payload and will not fly again, OSIRIS continues to collect data up to 82–90° latitude in both hemispheres and work is underway to interpret additional OH data from this valuable data set [Gattinger et al., 2008].

References

Bates, D. R., and M. Nicolet (1950), The photochemistry of atmospheric water vapor, *J. Geophys. Res.*, *55*(3), 301–327.

Bertaux, J.-L. (1986), The UV bright spot of water vapor in comets, *Astron. Astrophys.*, *160*, L7–L10.

Bertaux, J.-L., and A. Delannoy (1978), Vertical distribution of H_2O in the stratosphere as determined by UV fluorescence in-situ measurements, *Geophys. Res. Lett.*, *5*(12), 1017–1020.

Bevilacqua, R. M., et al. (1996), MAS measurements of the latitudinal distribution of water vapor and ozone in the mesosphere and lower thermosphere, *Geophys. Res. Lett.*, *23*(17), 2317–2320.

Boone, C. D., et al. (2005), Retrievals for the atmospheric chemistry experiment Fourier-transform spectrometer, *Appl. Opt.*, *44*(33), 7218–7231.

Brasseur, G. P., and S. Solomon (1986), *Aeronomy of the Middle Atmosphere*, 2nd ed., p. 238, Springer , New York.

Brueckner, G. E., et al. (1993), The Solar Ultraviolet Spectral Irradiance Monitor (SUSIM) experiment on board the Upper Atmosphere Research Satellite (UARS), *J. Geophys. Res.*, *98*(D6), 10,695–10,711.

Budzien, S. A., and P. D. Feldman (1991), OH prompt emission in comet IRAS-Araki-Alcock (1983 VII), *Icarus*, *90*, 308–318.

Burris, J., J. Butler, T. McGee, and W. Heaps (1991), Quenching and rotational transfer rates in the $v' = 0$ manifold of $OH(A^2\Sigma^+)$, *Chem. Phys.*, *151*, 233–238.

Cageao, R. P., et al. (1997), Calculated hydroxyl $A^2\Sigma \to X^2\Pi$ (0,0) band emission rate factors applicable to atmospheric spectroscopy, *J. Quant. Spectrosc. Radiat. Transfer*, *57*(5), 703–717.

Carrington, T. (1964), Angular momentum distribution and emission spectrum of OH $(A^2\Sigma^+)$ in the photodissociation of H_2O, *J. Chem. Phys.*, *41*, 2012–2018.

Chabrillat, S., and G. Kockarts (1997), Simple parameterization of the absorption of the solar Lyman-alpha line, *Geophys. Res. Lett.*, *24*(21), 2659–2662.

Chabrillat, S., and G. Kockarts (1998), Correction to ''Simple parameterization of the absorption of the solar Lyman-alpha line'', *Geophys. Res. Lett.*, *25*(1), 79.

Chidsey, I. L., and D. R. Crosley (1980), Calculated rotational transition probabilities for the A-X system of OH, *J. Quant. Spectrosc. Radiat. Transfer*, *23*, 187–199.

Chu, X., C. S. Gardner, and R. G. Roble (2003), Lidar studies of interannual, seasonal, and diurnal variations of polar mesospheric clouds at the South Pole, *J. Geophys. Res.*, *108*(D8), 8447, doi:10.1029/2002JD002524.

Cleary, D. D., S. Gnanalingam, R. P. McCoy, K. F. Dymond, and F. G. Eparvier (1995), The middle ultraviolet dayglow spectrum, *J. Geophys. Res.*, *100*(A6), 9729–9739.

Conway, R. R., et al. (1999), Middle atmosphere high resolution spectrograph investigation, *J. Geophys. Res.*, *104*(D13), 16,327–16,348.

Conway, R. R., et al. (2000), Satellite observations of upper stratospheric and mesospheric OH: The HO$_x$ dilemma, *Geophys. Res. Lett.*, *27*(17), 2613–2616.

Copeland, R. A., M. J. Dyer, and D. R. Crosley (1985), Rotational-level-dependent quenching of A $^2\Sigma^+$ OH and OD, *J. Chem. Phys.*, *82*, 4022–4032.

Coxon, J. A. (1980), Optimum molecular constants and term values for the $X^2\Pi(v \leq 5)$ and $A^2\Sigma^+(v \leq 3)$ states of OH, *Can. J. Phys.*, *58*, 933–949.

Crosley, D. R., and R. K. Lengel (1975), Relative transition probabilities and the electronic transition moment in the A-X system of OH, *J. Quant. Spectrosc. Radiat. Transfer*, *15*, 579–591.

Dieke, G. H., and H. M. Crosswhite (1962), The ultraviolet bands of OH, *J. Quant. Spectrosc. Radiat. Transfer*, *2*, 97–199.

Garcia, R. R. (1989), Dynamics, radiation, and photochemistry in the mesosphere: Implications for the formation of noctilucent clouds, *J. Geophys. Res.*, *94*, 14,605–14,615.

Gattinger, R. L., D. A. Degenstein, and E. J. Llewellyn (2006), Optical Spectrograph and Infra-Red Imaging System (OSIRIS) observations of mesospheric OH $A^2\Sigma^+–X^2\Pi$ 0-0 and 1-1 band resonance emissions, *J. Geophys. Res.*, *111*, D13303, doi:10.1029/2005JD006369.

Gattinger, R. L., D. A. Degenstein, E. J. Llewellyn, and M. H. Stevens (2008), OH $A^2\Sigma^+–X^2\Pi$ band ratios observed in the mesosphere by OSIRIS, *Can. J. Phys.*, in press.

Gumbel, J. (1997), Rocket-borne optical measurements of minor constituents in the middle atmosphere, Ph.D. thesis, 228 pp., Stockholm Univ., Sweden.

Harich, S. A., et al. (2000), Photodissociation of H$_2$O at 121.6 nm: A state-to-state dynamical picture, *J. Chem. Phys.*, *113*, 10,073–10,090.

Harries, J. E., et al. (1996), Validation of measurements of water vapor from the Halogen Occultation Experiment (HALOE), *J. Geophys. Res.*, *101*, 10,205–10,216.

Hervig, M., and D. E. Siskind (2006), Decadal and inter-hemispheric variability in polar mesospheric clouds, water vapor, and temperature, *J. Atmos. Sol. Terr. Phys.*, *68*, 30–41.

Hervig, M., M. McHugh, and M. E. Summers (2003), Water vapor enhancement in the polar summer mesosphere and its relationship to polar mesospheric clouds, *Geophys. Res. Lett.*, *30*(20), 2041, doi:10.1029/2003GL018089.

Kaneko, M., Y. Mori, and I. Tanaka (1968), Electronic quenching and the rotational relaxation rate of OH*($^2\Sigma^+$) produced by the vacuum-ultraviolet photodecomposition of water, *J. Chem. Phys.*, *48*(10), 4468–4473.

Kelly, K. K., et al. (1993), Water vapor and cloud water measurements over Darwin during the STEP 1987 tropical mission, *J. Geophys. Res.*, *98*(D5), 8713–8723.

Khaplanov, M., J. Gumbel, N. Wilhelm, and G. Witt (1996), Hygrosonde - A direct measurement of water vapor in the stratosphere and mesosphere, *Geophys. Res. Lett.*, *23*(13), 1645–1648.

Kley, D., et al. (1979), In situ measurements of the mixing ratio of water vapor in the stratosphere, *J. Atmos. Sci.*, *36*, 2513–2524.

Kohl, J. L., W. H. Parkinson, and R. L. Kurucz (1978), Center and Limb Solar Spectrum in High Spectral Resolution 225.2 to 319.6 nm, 236–249 pp., Harvard Univ., Cambridge, Mass.

Lambert, A., et al. (2007), Validation of the aura microwave limb sounder middle atmosphere water vapor and nitrous oxide measurements, *J. Geophys. Res.*, *112*, D24S36, doi:10.1029/2007JD008724.

Lee, L. C., and M. Suto (1986), Quantitative photoabsorption and fluorescence study of H$_2$O and D$_2$O at 50–190 nm, *Chem. Phys.*, *110*, 161–169.

Lee, L. C., L. Oren, E. Phillips, and D. L. Judge (1978), Cross sections for production of the OH($A^2\Sigma^+ \rightarrow X^2\Pi$) fluorescence by photodissociation of H$_2$O vapour, *J. Phys. B At. Mol. Opt. Phys.*, *11*(1), 47–54.

Lewis, B. R., I. M. Vardavas, and J. H. Carver (1983), The aeronomic dissociation of water vapor by solar H Lyman α radiation, *J. Geophys. Res.*, *88*(A6), 4935–4940.

Llewellyn, E. J., et al. (2004), The OSIRIS instrument on the Odin spacecraft, *Can. J. Phys.*, *82*, 411–422.

Luque, J., and D. R. Crosley (1998), Transition probabilities in the A $^2\Sigma^+–X^2\Pi_i$ electronic system of OH, *J. Chem. Phys.*, *109*(2), 439–448.

McHugh, M., et al. (2003), Improved mesospheric temperature, water vapor and polar mesospheric cloud extinctions from HALOE, *Geophys. Res. Lett.*, *30*(8), 1440, doi:10.1029/2002GL016859.

McHugh, M., et al. (2005), Comparison of atmospheric retrievals from ACE and HALOE, *Geophys. Res. Lett.*, *32*, L15S10, doi:10.1029/2005GL022403.

Michelsen, H. A., et al. (2002), ATMOS version 3 water vapor measurements: Comparisons with observations from two ER-2 Lyman-α hygrometers, MkIV, HALOE, SAGE II, MAS, and MLS, *J. Geophys. Res.*, *107*(D3), 4027, 10.1029/2001JD000587.

Milz, M. T., et al. (2005), Water vapor distributions measured with the Michelson Interferometer for Passive Atmospheric Sounding on board Envisat (MIPAS/Envisat), *J. Geophys. Res.*, *110*, D24307, doi:10.1029/2005JD005973.

Murtagh, D., et al. (2002), An overview of the Odin atmospheric mission, *Can. J. Phys.*, *80*, 309–319.

Nicolet, M. (1984), On the photodissociation of water vapour in the mesosphere, *Planet. Space Sci.*, *32*(7), 817–880.

Okabe, H. (1980), Photodissociation of nitric acid and water in the vacuum ultraviolet: Vibrational and rotational distributions of OH$^2\Sigma^+$, *J. Chem. Phys.*, *72*, 6642–6650.

Papagiannakopoulos, P., and C. Fotakis (1985), Kinetic studies of OH($A^2\Sigma^+$) generated by two-photon excitation of H$_2$O at 248 nm, *J. Phys. Chem.*, *89*, 3439–3441.

Picone, J. M., A. E. Hedin, D. P. Drob, and A. C. Aikin (2002), NRLMSISE-00 empirical model of the atmosphere: Statistical comparisons and scientific issues, *J. Geophys. Res.*, *107*(A12), 1468, doi:10.1029/2002JA009430.

Pumphrey, H. C. (1999), Validation of a new prototype water vapor retrieval for the UARS Microwave Limb Sounder, *J. Geophys. Res.*, *104*(D8), 9399–9412.

Rottman, G. J., T. N. Woods, and T. P. Sparn (1993), Solar-Stellar Irradiance Comparison Experiment 1: 1. Instrument design and operation, *J. Geophys. Res.*, *98*(D6), 10,667–10,677.

Rouse, P. E., and R. Engleman (1973), Oscillator strengths from line absorption in a high-temperature furnace. part I: The (0,0) and (1,0) bands of the $A^2\Sigma^+–X^2\Pi_i$ transition in OH and OD*, *J. Quant. Spectrosc. Radiat. Transfer*, *13*, 1503–1521.

Russell, J. M., III, et al. (1993), The Halogen Occultation Experiment, *J. Geophys. Res.*, *98*(D6), 10,777–10,797.

Schleicher, D. G., and M. F. A'Hearn (1988), The fluorescence of cometary OH, *Astrophys. J.*, *331*, 1058–1077.

Schwab, J. J., E. M. Weinstock, J. B. Nee, and J. G. Anderson (1990), In situ measurement of water vapor in the stratosphere with a cryogenically cooled Lyman-Alpha hygrometer, *J. Geophys. Res.*, *95*(D9), 13,781–13,796.

Siskind, D. E., M. H. Stevens, and C. R. Englert (2005), A model study of global variability in mesospheric cloudiness, *J. Atmos. Sol. Terr. Phys.*, *67*, 510–513.

Smith, A. K., and G. P. Brasseur (1991), Numerical simulation of the seasonal variation of mesospheric water vapor, *J. Geophys. Res.*, *96*(D4), 7553–7563.

Stark, G., J. W. Brault, and M. C. Abrams (1994), Fourier-transform spectra of the $A^2\Sigma^+$-$X^2\Pi$ $\Delta v = 0$ bands of OH and OD, *J. Opt. Soc. Am. B Opt. Phys.*, *11*(1), 3–32.

Stevens, M. H., and R. R. Conway (1999), Calculated OH $A^2\Sigma^+$-$X^2\Pi$ (0,0) band rotational emission rate factors for solar resonance fluorescence, *J. Geophys. Res.*, *104*(D13), 16,369–16,378.

Stevens, M. H., C. R. Englert, M. T. DeLand, and S. M. Bailey (2007), Polar mesospheric cloud mass and the ice budget: 2. Application to satellite data sets, *J. Geophys. Res.*, *112*, D08205, doi:10.1029/2006JD007532.

Terenin, A., and H. Neujmin (1934), Photodissociation of molecules in the Schumann ultra-violet, *Nature*, *134*, 255.

Vikis, A. C. (1978), The OH ($A^2\Sigma^+$) internal energy distribution produced by the Kr($^3P_1$) sensitized decomposition of H$_2$O, *J. Chem. Phys.*, *69*, 4314–4316.

Woods, T. N. et al. (1996), Validation of the UARS solar ultraviolet irradiances: Comparison with the ATLAS 1 and 2 measurements, *J. Geophys. Res.*, *101*(D6), 9541–9569.

————————————

D. A. Degenstein, R. L. Gattinger, and E. J. Llewellyn, ISAS, Department of Physics and Engineering Physics, University of Saskatchewan, 116 Science Place, Saskatoon, SK, Canada S7N 5E2.

J. Gumbel, M. Khaplanov, and G. Witt, Department of Meteorology, Stockholm University, 10691 Stockholm, Sweden.

M. H. Stevens, Space Science Division, Naval Research Laboratory, Code 7641, 4555 Overlook Avenue, SW, Washington, DC 20375, USA. (michael.stevens@nrl.navy.mil)